AGU PUBLICATIONS

JGR

Journal of Geophysical Research: Atmospheres

RESEARCH ARTICLE
10.1002/2017JD027884

This article is a companion to Zhang and Tinsley (2017), https://doi.org/10.1002/2016JD026255.

Key Points:
- Atmospheric electric charge affects particle scavenging rates in clouds
- Extensive simulations add particle density variations to those for relative humidity given previously for 3 μm radius droplets
- The results have been parameterized for incorporation into cloud models

Supporting Information:
- Text S1
- Data Set S1
- Table S1
- Text S2
- Table S2

Correspondence to:
B. A. Tinsley,
tinsley@utdallas.edu;
liangzhang@geo.ecnu.edu.cn

Citation:
Zhang, L., & Tinsley, B. A. (2018). Parameterization of in-cloud aerosol scavenging due to atmospheric ionization: 2. Effects of varying particle density. *Journal of Geophysical Research: Atmospheres*, *123*, 3099–3115. https://doi.org/10.1002/2017JD027884

Received 6 JUN 2017
Accepted 2 JAN 2018
Accepted article online 9 JAN 2018
Published online 22 MAR 2018

Parameterization of In-Cloud Aerosol Scavenging Due To Atmospheric Ionization: 2. Effects of Varying Particle Density

Liang Zhang[1,2] and Brian A. Tinsley[2]

[1]Institute of Eco-Chongming, East China Normal University, Shanghai, China, [2]Physics Department, University of Texas at Dallas, Richardson, TX, USA

Abstract Simulations and parameterization of collision rate coefficients for aerosol particles with 3 μm radius droplets have been extended to a range of particle densities up to 2,000 kg m^{-3} for midtropospheric (~5 km) conditions (540 hPa, −17°C). The increasing weight has no effect on collisions for particle radii less than 0.2 μm, but for greater radii the weight effect becomes significant and usually decreases the collision rate coefficient. When increasing size and density of particles make the fall speed of the particle relative to undisturbed air approach to that of the droplet, the effect of the particle falling away in the stagnation region ahead of the droplet becomes important, and the probability of frontside collisions can decrease to zero. Collisions on the rear side of the droplet can be enhanced as particle weight increases, and for this the weight effect tends to increase the rate coefficients. For charges on the droplet and for large particles with density $\rho < 1{,}000$ kg m^{-3} the predominant effect increases in rate coefficient due to the short-range attractive image electric force. With density ρ above about 1,000 kg m^{-3}, the stagnation region prevents particles moving close to the droplet and reduces the effect of these short-range forces. Together with previous work, it is now possible to obtain collision rate coefficients for realistic combinations of droplet charge, particle charge, droplet radius, particle radius, particle density, and relative humidity in clouds. The parameterization allows rapid access to these values for use in cloud models.

Plain Language Summary Atmospheric electric charges affect the rate of collision with droplets of aerosol particles acting as condensation nuclei and ice-forming nuclei. This changes their concentrations and can generate primary ice, affecting the development of clouds, and explains observations of cloud and surface pressure responses to changes in atmospheric electricity. We have modeled these collision rates as functions of electric charges, particle radii and density, and relative humidity, extending previous results for a range of droplet radii. We give the results in a form easily incorporated into cloud models.

1. Introduction

1.1. Atmospheric Relevance

Electric charges on droplets and aerosol particles in clouds cause size-dependent changes in collision rates and thus in collection rates of aerosol particles (in-cloud scavenging) (Pruppacher & Klett, 1997). Under some conditions such charge effects may result in changes in the concentrations and size distributions of cloud condensation nuclei (CCN) and ice-nucleating particles (INP) both within clouds and in air masses after the clouds dissipate or precipitate. A scenario for this involves the space charge that is generated at cloud boundaries when the current density (*Jz*) in the global electric circuit flows downward through the conductivity gradients at the boundaries of clouds, in accordance with Poisson's equation (Zhou & Tinsley, 2007). The space charge consists of an excess of charge of one sign and the charges attach to aerosol particles and droplets. For small particles the same sign charges on droplets and particles tend to reduce collision rates due to the long-range repulsive Coulomb force (Tinsley, 2010; Tinsley et al., 2006). We call this reduction in collision rates electroantiscavenging. For opposite signs of charges on droplets and small particles the collision rates are increased; however, in the space charge regions the net effect of the greater concentration of same sign charges is a decrease in scavenging rates.

For large particles, irrespective of the signs of the particles and droplets, the particle charges tend to increase the collision rates, due to the short-range image electric force (Zhang & Tinsley, 2017; Zhou et al., 2009). Thus, even in cloud interiors in the absence of space charge, with equal numbers of charged aerosol particles of

both signs present, the collision rates for the larger aerosol particles will increase. We call such increases in rates electroscavenging. The electroscavenging and electroantiscavenging effects are together called "charge modulation of aerosol scavenging" or CMAS (Tinsley, 2010).

Excluding the enormous amounts of charge generated in thunderstorms, the largest amounts of space charge are found at the upper and lower boundaries of stratus clouds, the upper boundaries of layers of haze and sea-salt aerosol over the oceans, and the upper boundary of tropospheric mixing. The thickness of the layers and the dilution of the space charge depend on the strength of mixing at the boundaries. Recent models and observations of cloud charging have been given by Zhou and Tinsley (2007, 2012) and by Nicoll and Harrison (2016); in addition, there is an extensive review by Pruppacher and Klett (1997).

Changes in scavenging rates affect the concentrations and size distributions of CCN and INP, by cumulative losses with electroscavenging or cumulative gains with electroantiscavenging compared to the reductions that would otherwise have appeared with Brownian and/or phoretic scavenging. Lifetimes for such changes can be estimated from the collision rate coefficients, as in Tinsley (2010, section 8 and Table 1).

Although no quantitative models have been constructed, it was suggested by Zhou et al. (2017) that electroantiscavenging of ultrafine aerosol particles could provide an explanation for the increases in polar cloud cover associated with observed pressure variations correlated with *Jz* changes. For stratus clouds changes in the concentration of CCN can cause significant changes in cloud cover (Rosenfeld et al., 2006; Twomey, 1977). Statistical evidence has been advanced for responses of Antarctic and Arctic meteorology to *Jz* changes, including those induced by the solar wind (Burns et al., 2008; Kniveton et al., 2008; Lam et al., 2013, 2014, 2017; Zhou et al., 2017). The correlations of Arctic and Antarctic cloud cover opacity changes by Frederick (2016, 2017) with magnetic activity are also correlations with *Jz* changes in those regions associated with auroral current systems (Frank-Kamenetsky et al., 2012). The day-to-day timescale of these correlations and the fact that they have the same sensitivity to the external solar wind-induced *Jz* changes as to the internal thunderstorm-induced *Jz* changes (Burns et al., 2008) renders implausible explanations other than electrically induced changes in cloud microphysics.

It was suggested by Tinsley (2012) that some or all of increases in electroantiscavenging of small CCN, electroscavenging of large CCN, and electroscavenging of contact ice nuclei could provide an explanation for observed correlations of winter storm vorticity with changes in *Jz*. These correlations may be due to storm invigoration (Rosenfeld et al., 2008; Tinsley, 2012; Tinsley & Yu, 2004). For contact ice nucleation, the work of Yang et al. (2015) adds to that of Abbas and Latham (1969) discussed by Tinsley and Dean (1991), suggesting that liquid shear in the strong electric fields between the charged particle and its image, at the moment of contact of a charged INP with a supercooled droplet, may further increase the efficiency and thus the amount of contact ice nucleation.

Within updrafts the collection rates of INP acting as contact ice nuclei (above the freezing level) or as immersion nuclei (when later carried above the freezing level) are negligible when only diffusion and the repulsive phoretic force (that acts with relative humidity (RH) greater than 100%) are considered (Young, 1993, section 4.5.3). (Immersion nucleation involves INP that are collected at temperatures too high for freezing but that initiate freezing when the liquid droplet is cooled down sufficiently and together with contact nucleation are defined by Vali (1985) and Ladino et al., (2013). Thus, electric charges on the INP can significantly increase the electroscavenging and therefore collection rates for immersion and contact nucleation in updrafts, as we showed in Zhang and Tinsley (2017) and shown in section 3.3 of this work.

In previous work simulations and parameterizations were made for particle density ρ = 500 kg m^{-3} for droplets of 3 μm radius (Zhang & Tinsley, 2017) and also for 6 μm and 15 μm radii droplets (Tinsley & Leddon, 2013; Tinsley & Zhou, 2015). Generally, the simulations have been made, as in this work, for midtropospheric (~5 km) conditions (540 hPa, −17°C), but simulations for altitudes from the surface to 20 km were made by Tinsley and Leddon (2013). For the higher-particle densities and the 3 μm radius droplets considered in this work the interactions are more complex, due to the smaller differences in fall speeds and the larger effect of the flow around the particle (fap) on the droplet trajectories.

In this work, we continue to investigate the CMAS effects as a function of particle density for the smaller droplets and the larger particle sizes, such as the larger and more effective and higher-density mineral INP with their greater numbers of nucleation sites (Ladino et al., 2013). We provide accurate parameterizations of the results and in addition approximations where they may be useful. This work

extends the previous work on CMAS for larger droplets to a lower range of droplet sizes. It makes possible, for use in cloud models, more of the full range of droplet sizes and particle densities involved in in-cloud scavenging.

2. Basic Theory and Methods

2.1. Development From Previous Work

In this work we apply a Monte Carlo trajectory model to calculate the collision rate coefficient, using the trajectory model with Brownian diffusion, which has continually evolved (Tinsley, 2010; Tinsley & Leddon, 2013; Tinsley & Zhou, 2015; Zhang, 2017; Zhang & Tinsley, 2017) and which now includes effects of weight, intercept, fap, phoretic forces, electric forces, and diffusion. The Brownian diffusion is simulated by Monte Carlo selection of three random numbers to give increments of displacement in three dimensions, as described by Tinsley (2010, sections 2 and 3). The electric forces in this model include image electric forces as well as the Coulomb force and are as given by Davis (1964a, 1964b) and Khain et al., (2004) with the several approaches that have been used compared in Zhou et al. (2009, section 3.1 and Figure 1). Formulas for the variation of the thermophoretic and diffusiophoretic forces with RH are given in Appendix A of Tinsley et al. (2006), based on Pruppacher and Klett (1997) (see also Davenport & Peters, 1978). These are not the same as those that are often used, for example, as given by Andronache et al. (2006) or Wang et al. (2010), where in their equation A3 the parameter α_{th} incorrectly uses the droplet diameter instead of the particle diameter for the Knudsen number.

The air flow around the droplets and particles is given by a merging of the Proudman and Pearson and Oseen flow fields (Tinsley et al., 2006). For the effects of fap on the droplet trajectory we use the superposition approach (Langmuir, 1948; Tinsley et al., 2006) as will be discussed in a later section. These effects are considerable when the particle sizes are comparable to those of the droplets and hence important for the collision rates of micron-sized particles with the 3 μm droplets in this paper. For the slow fall speeds and slow encounters between the objects only a few microns in size, the inertial effects are negligible and are not included. We express the results of our trajectory simulations as collision rate coefficients in units of $m^3\ s^{-1}$, which when multiplied by the concentration of the droplets and the concentration of the particles gives the rate of collisions per unit volume per unit time ($m^{-3}\ s^{-1}$). With our Monte Carlo approach to determine the probability of collisions, this definition arises (Tinsley, 2010, section 4) by a summation over the probabilities for collision, for particle trajectories starting from points below the droplet, as functions of increasing offsets from a vertical axis through the droplet center. Its use is equivalent to, and combines, the use of collision kernel, collision efficiency, and swept volume (Pruppacher & Klett, 1997).

2.2. Effects of Particle Density for Large Particles and Small Droplets

2.2.1. Fall Speed of Droplets and Particles

The density of particles with radius greater than 1.25 μm near the Earth's surface is dependent on particle species, and Hand and Kreidenweis (2002) showed that the average value of retrieved effective density for near-surface particles in Southwest Texas was 1.85 ± .14 g cm^{-3} or 1,850 kg m^{-3}. In the atmosphere and in clouds, aerosol particles can exist in both liquid and solid forms, for example, the density of liquid sulfuric acid is 1,100 to 1,800 kg m^{-3}, depending on concentration. For organic carbon the density is about 1,400 kg m^{-3}, for silicate particles about 2,000 kg m^{-3}, and for sea salt about 2,100 kg m^{-3} (Hand & Kreidenweis, 2002, and references therein). If the shape of particles is irregular and elongated, then the effective density could be as low as 500 kg m^{-3} (Pruppacher & Klett, 1997). In our model, five values of particle density ρ are applied: 1, 500, 1,000, 1,500, 2,000 kg m^{-3}. We include the case of particle density $\rho = 1$ kg m^{-3}, which is not realistic, in order to show the collision rate coefficient in the absence of the effect of weight.

Aerosol particles fall in air due to gravity, and for particles of radius a, a constant fall speed relative to undisturbed air, $U_{a,\infty}$, is reached when the drag force is equal to their gravitational force mg, where m is the mass of the particle and g is the gravitational acceleration. The drag force is given by

$$\vec{F}_{\text{drag}} = \frac{\vec{v_f} - \vec{v}}{B_p(a)} \tag{1}$$

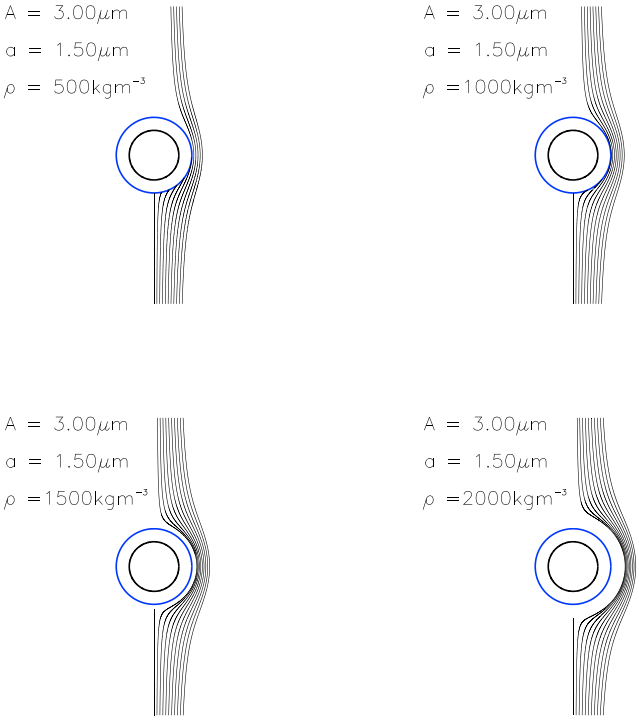

Figure 1. Trajectories of 1.5 μm particles around 3.0 μm droplets for particle density ρ = 500, 1,000, 1,500, and 2,000 kg m^{-3} and no diffusion. The inner black circle represents the droplet, and the outer blue circle corresponds to the sum of droplet and particle radius. As the particle density increases its fall speed approaches that of the droplet and the particle does not penetrate a "stagnation" region of low flow speed around the droplet, but is diverted to the side, reducing the collision rate. For the 1,500 and 2,000 kg m^{-3} particles the collision rate becomes zero.

where $\vec{v_f}$ is the velocity of air flow, $\vec{v}$ is the velocity of the particle, and $B_p(a)$ is the mobility of the particle (Tinsley et al., 2006). Thus, the fall speed of the particle relative to undisturbed air is

$$U_{a,\infty} = B_p(a)mg \tag{2}$$

The fall speed of droplet relative to undisturbed air $U_{A,\infty}$ can also be obtained by replacing the particle radius a and mass m with droplet radius A and mass M and mobility of the droplet B_d (A) in equation (2).

For particles with radius 0.1 μm $\leq a \leq$ 3.0 μm, the particle mobility is roughly inversely proportional to radius, $B_p(a) \propto 1/a$, and so that the fall speed of particle relative to undisturbed air is approximately proportional to particle density ρ and the square of particle radius, $U_{a,\infty} \propto \rho a^2$. The fall speed of the particle relative to undisturbed air $U_{a,\infty}$ approaches the droplet's fall speed $U_{A,\infty}$ when the particle radius a approaches the value of $A\sqrt{1,000/\rho}$. If the particle radius continues to increase, its fall speed in undisturbed air could exceed that of the droplet, in which case it could not be overtaken by the droplet. Therefore, in our model the maximum radius of the particle is set to be 2.3 μm for a particle with density of 1,500 kg m^{-3} and set to be 2.0 μm for a particle with density of 2,000 kg m^{-3}.

2.2.2. Stagnation Region and Rear Capture

In our trajectory model, the coordinate system is centered on the falling droplet, so that in this frame, the air flows upward around the droplet. The speed of air flow is $U_{A,\infty}$ far from the droplet and gradually decreases toward the droplet, until it reaches zero at the droplet surface. The particles are released below the droplet and then move upward with the flow and through the flow to the extent that any forces are present. If only the gravitational force is present, then according to equations (1) and (2), we have

$$\left|\vec{v_f} - \vec{v}\right| = U_{a,\infty} \tag{3}$$

The velocity of air flow $\vec{v_f}$ is roughly equal to the fall speed of droplet $U_{A,\infty}$ relative to undisturbed air except for the position very close to droplet surface; thus,

$$\frac{|\vec{v_f} - \vec{v}|}{|\vec{v_f}|} \approx \frac{U_{a,\infty}}{U_{A,\infty}} \tag{4}$$

As the particle radius decreases the fall speed of the particle $U_{a,\infty}$ decreases rapidly and consequently if the particle radius is small enough that the right side of equation (4) will be negligible and the particle velocity $\vec{v}$ will be very close to the velocity of air flow $\vec{v_f}$; thus, for very small particles the trajectories without diffusion will coincide with the flow lines, and the diffusion of particles is independent of particle density; therefore, the collision rate coefficients for small particles do not depend on particle density. In the presence of electrical and phoretic forces the particle motion departs from the flow lines, and this departure is also independent of particle density.

However, for large particles the trajectories without diffusion will depart from the flow lines if the weight of particle is considerable, and normally, the weight effect will reduce the collision rate coefficient through pulling the particle away from the droplet. Figure 1 illustrates the trajectories of 1.5 μm particles around a 3.0 μm droplet in the absence of electric forces, phoretic forces, and diffusion, with particle densities ρ from 500 to 2,000 kg m^{-3}. The inner circle represents the droplet radius, the outer circle corresponds to the sum of droplet and particle radii, and the particle will collide with the droplet when the trajectories reach the outer circle.

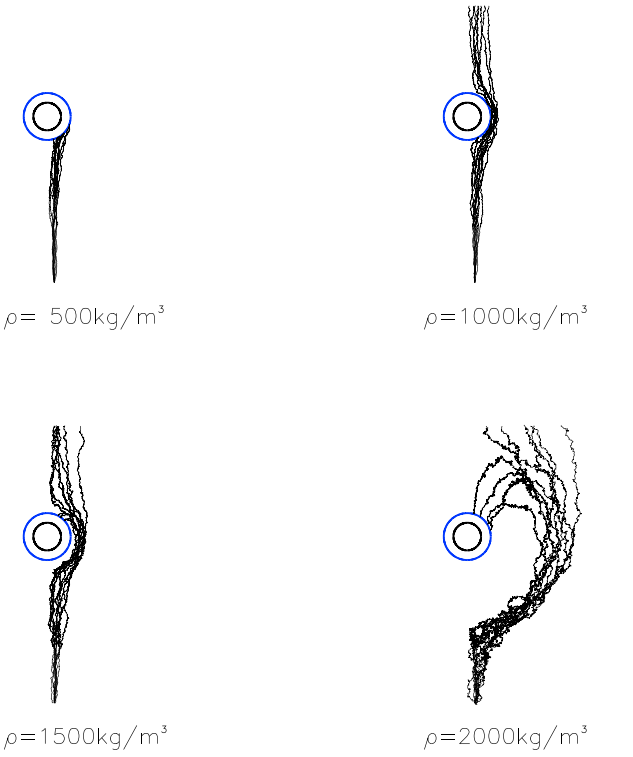

Figure 2. Trajectories of 2.0 μm particles around 3.0 μm droplets with inclusion of diffusion, with particle density ρ = 500, 1,000, 1,500, and 2,000 kg m^{-3} respectively. The effects of diffusion are to move particles across flow lines so that the weight of the particle then allows it to fall toward the droplet on the backside, in the low flow speed region.

In the coordinates of the droplet, the speed of air flow will decrease to zero at the droplet surface, and immediately below the droplet there must exist a stagnation point where the upward air flow is reduced sufficiently that the particle falls at the same speed as the droplet; that is, it comes to rest relative to the droplet. Between it and the droplet there is a stagnation region within which the upward drag force on the particle at rest relative to the droplet is less than the particle weight and into which particles could not enter without diffusion, inertia, or attractive forces, so that the stagnation region prevents particles from colliding on the front side of droplet and the flow diverts them to the side. As shown in Figure 1, for particles with density of 500 kg m^{-3} the trajectories are roughly aligned with flow lines as the weight of particles is small, and collisions occur at the front side of droplet. As the particle density increases, the trajectories of particles fall across the flow lines due to the increasing weight, and it is more difficult for particles to collide at the front side of droplet. For particles with higher density the particle could not collide on the front surface of droplet without diffusion, as shown by the cases for particles with density of 1,500 and 2,000 kg m^{-3} in Figure 1. Tinsley et al. (2006) have investigated the effect of the stagnation region in consideration of the weight and inertia (not important for A = 3 μm) of particles and electric forces for A = 20 μm droplets.

When particles are carried into the low flow region behind the falling droplet, the gravitational force will move the particle toward the droplet. In the presence of diffusion, particles can enter the low flow region through random movement, and with the downward gravitational force it can collide with the rear side of droplet. Figure 2 illustrates the trajectories of particles around a droplet in consideration of diffusion, with droplet radius A = 3.0 μm, particle radius a = 2.0 μm, and particle densities ρ from 500 to 2,000 kg m^{-3}. It can be seen that collisions occur at the front side of droplet for particle density $\rho <$ 1,000 kg m^{-3} and at the rear side for $\rho \geq$ 1,000 kg m^{-3}. The process of rear-side collision is quite nonlinear and increases the collision rate coefficient for increasing particle weight. When the fall speed of the particle increases toward that of the droplet, the relative speed between droplet and particle becomes smaller, and more time is needed for the droplet to encounter the particles released below; in other words, there is more time for diffusion which allows some of the particles to traverse the flow lines and fall into the low flow region, and in this way increase the collision rate coefficient.

2.2.3. Flow Around the Particle (fap)

In our Monte Carlo Trajectory Model the effects of the drag force on the droplet exerted by fap are considered, as well as the intercept effect and the electric, phoretic, and gravitational forces. The superposition method (Langmuir, 1948) is used to simulate fap. This approach was used by Tinsley et al. (2006, section 2 and Figures 1, 2, and 5), with the coordinates of the droplet center as affected by the stream function around the particle being adjusted alternately with the coordinates of the particle center as affected by the stream function around the droplet.

The control function of the droplet is

$$m_1 \frac{d\vec{v}}{dt} = \frac{\vec{v_f} - \vec{v}}{B_d(A)} + \vec{f_e} + \vec{f_g} \tag{5}$$

where m_1 is the mass of the droplet, $\vec{v}$ is the velocity of the droplet, $\vec{v_f}$ is the disturbance of air flow caused by the particle, $B_d(A)$ is the droplet mobility, $\vec{f_e}$ are the electric forces, and $\vec{f_g}$ is the gravitational force. Assuming that the inertia of the droplet is negligible so that the left-hand side of (5) can be taken as zero and that the electric forces are negligible, then the velocity of the droplet is

$$\vec{v} = \vec{v_f} + \vec{U}_{A,\infty} \tag{6}$$

where $U_{A,\infty} = f_g B_p(A)$ is the fall speed of the droplet relative to the undisturbed air. When the particle is far away from the droplet, the disturbance of air flow $\vec{v_f}$ is negligible, so that the speed of droplet is equal to

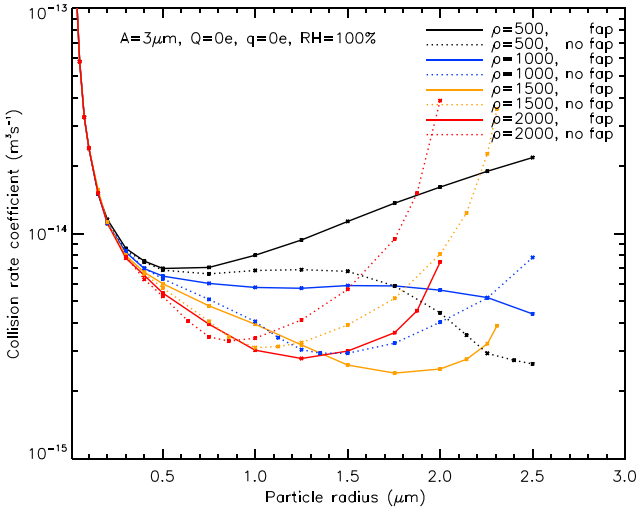

Figure 3. Effects of flow around the particle (fap) and density in the absence of charges and phoretic effects. Collision rate coefficients $R_{0,0,100\%,\rho}$ ($m^3\ s^{-1}$) calculated without fap (dashed lines) and with fap (solid lines), with particle density ρ = 500, 1,000, 1,500, and 2,000 kg m^{-3} respectively. The large increase in collision rate coefficient due to fap for ρ = 500 kg m^{-3} is for all particle radii but is reduced to successively smaller ranges of particle radii as the density increases. Thus, for ρ = 2,000 kg m^{-3} the increase is present only between 0.4 and 0.9 μm particle radii. The nonlinear rate increases for larger radii and densities are due to increasing weight, fap, and rear collisions as the particle fall speeds approach that of the droplet.

$U_{A,\infty}$. When the droplet and the particle are close, if we assume that the disturbance of air flow $\vec{v_f}$ is similar as the fall speed of the particle relative to undisturbed air $U_{a,\infty}$, then the relative disturbance of droplet velocity caused by the flow around particle is roughly

$$\frac{\left|\vec{v} - \vec{U}_{A,\infty}\right|}{\left|\vec{U}_{A,\infty}\right|} \approx \frac{U_{a,\infty}}{U_{A,\infty}} \tag{7}$$

According to equation (7), if the fall speed of the particle $U_{a,\infty}$ is much smaller than the fall speed of the droplet $U_{A,\infty}$, then the fap effect can be neglected. In our model, we neglect the fap effect when the relative disturbance is less than 1%. Due to the fall speed of the droplet and particle relative to undisturbed air being approximately proportional to the square of their radii, the fap usually starts to take effect when the particle radius is larger than 10% of the droplet radius.

Figure 3 shows the collision rate coefficient calculated by our Monte Carlo Trajectory Model, in the absence of electric and phoretic forces and with and without fap, by the solid and dashed lines, for particles with density ranging from 500 to 2,000 kg m^{-3}. We can see that the fap effect is negligible for $a < 0.3$ μm for all particle densities. When $a > 0.3$ μm and for particles with density of 500 kg m^{-3}, the collision rate coefficient with fap is always greater than without fap, and the difference is greater for larger particle radii. This is because the drag force exerted on the droplet caused by fap tends to drag the droplet downward. As shown in Figure 2, the collision occurs at the front side of droplet for particle density less than that of the droplet, so that the fap effect drags the droplet toward the particle and enhances the collision rates, and the larger the particle radius the greater the fap effect becomes. But for particles with density 1,000 kg m^{-3} to 2,000 kg m^{-3} the collision rate coefficient with fap will first tend to be greater than that without fap for the same reason as for the 500 kg m^{-3} particles; that is, the collision occurs at the front side of droplet for small particles with large density. However, as shown in Figure 3, as the particle radius becomes larger the collision rate coefficient with fap tends to be smaller than without fap. There are two contributing effects, one is that the drag force exerted on the droplet caused by fap is always downward and for a larger particle with larger density the collision mainly occurs at the rear side of the droplet, and the drag force tends to push the droplet away from the particle and thus decreases the collision rate coefficients. The second effect is that for particles with larger radius and larger density, their fall speed $U_{a,\infty}$ approaches that of the droplet $U_{A,\infty}$, and so the relative speed is small and there is more time for random Brownian diffusion to transport the particle close to the droplet. So diffusion tends to increase the collision rate coefficient. However, the fap effect tends to increase the relative speed between the droplet and particles and so decreases the time for diffusion, making the collision rate coefficient with fap smaller than without fap in these cases.

2.3. Input Values and Approach to Parameterization

In the previous paper (Zhang & Tinsley, 2017), the collision rate coefficients obtained with the trajectory model are designated as $R_{Q,q,A,a,\mathrm{RH}}$ (where Q is the droplet charge, q is the particle charge, A is the droplet radius, a is the particle radius, and RH is the relative humidity). For convenience, in that work the collision rate coefficient is abbreviated as $R_{Q,q,\mathrm{RH}}$. The particle density ρ in previous work was fixed at 500 kg m^{-3}, and in this paper we evaluate the collision rate coefficient for an extended range of particle density, for midtropospheric conditions P = 540 hPa, and T = 256.15 K as before. Now the collision rate coefficients are designated as $R_{Q,q,A,a,\mathrm{RH},\rho}$ and abbreviated as $R_{Q,q,\mathrm{RH},\rho}$. The values of ρ used were 1, 500, 1,000, 1,500, and 2,000 kg m^{-3}. The value of A used was 3 μm, while the values of a used were 0.2, 0.3, 0.4, 0.5, 0.75, 1.0, 1.25, 1.5, 1.75, 2.0, 2.25, and 2.5 μm for particle density less than or equal to 1,000 kg m^{-3}, while the maximum values of a were 2.3 and 2.0 μm for particle densities of 1,500 and 2,000 kg m^{-3}, respectively. The particle charges q were 0e, 10e, 20e, and 50e, and the droplet charges Q were 0e, ±10e, ±20e, ±50e, and ±100e, where e is the elementary charge. The values of RH were 95%, 98%, 99%, 100%, and 101%. For $a < 0.2$ μm the effect of particle weight is

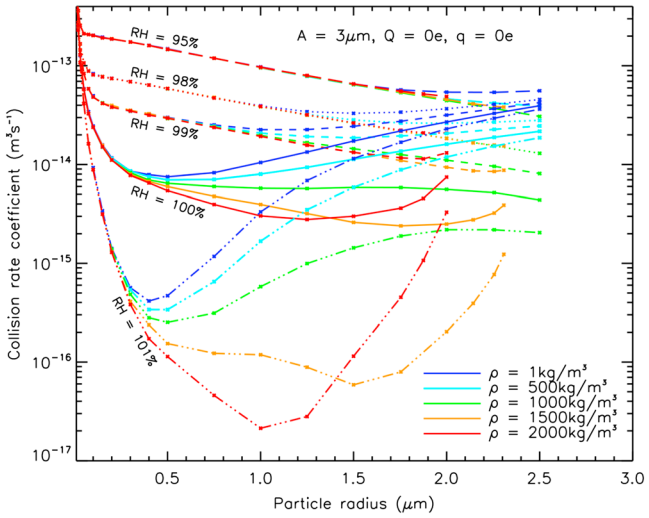

Figure 4. Effects of density and relative humidity (RH) in the absence of charges. Simulated collision rate coefficients $R_{0,0,RH,\rho}$ with RH = 95%, 98%, 99%, 100%, and 101% and particle density ρ = 1, 500, 1,000, 1,500, and 2,000 kg m^{-3}. The separation of the families of RH curves on the left is the effect of the phoretic forces. The separation within the RH families in the center and right and the crossover for the curves for density 2,000 kg m^{-3} at RH 100% and 101% are due to the increasing weight, flow around the particle, and rear collisions as the particle fall speeds approach that of the droplet.

negligible so the results of the previous work for particle density of 500 kg m^{-3} have been utilized, as given in Tables A1 to A5 in Zhang and Tinsley (2017).

The computational uncertainties of the collision rate coefficient in present simulations are less than 1% for most cases, except for limiting cases of high particle density and strong repulsive force for which the collision rate coefficients are small. Because of computing time limitations, it is impractical to further reduce the uncertainty by increasing the number of trials.

The collision rate coefficients $R_{Q,q,A,a,RH,\rho}$ are affected by as many as six of the variables Q, q, A, a, RH, and ρ, and it would be an enormous amount of work to calculate the rate coefficient separately for each combination of variables while running cloud models. Parameterization of the collision rate coefficients as a function of these variables was initiated by the work of Tinsley and Leddon (2013) and Tinsley and Zhou (2015) who parameterized the simulated results of $R_{Q,q,A,a,100\%,500}$, that is, for varying Q, q, A, a, RH = 100%, and ρ = 500 kg m^{-3}. Zhang and Tinsley (2017) extended the simulations for RH variations 95% to 101% for droplet radius A = 3.0 μm and parameterized the simulated results of $R_{Q,q,3,a,RH,500}$. In the present work, we extend the simulations for a range of particle densities 1 to 2,000 kg m^{-3} and parameterize the collision rate coefficients for $R_{Q,q,3,a,RH,\rho}$. In future work with particle density variations, we plan to extend the values of droplet radius and fully parameterize the collision rate coefficients for $R_{Q,q,A,a,RH,\rho}$.

To parameterize the collision rate coefficients, we first fit the simulated results of collision rate coefficient $R_{0,0,RH,\rho}$ for zero droplet charge and zero particle charge as a function of a, RH, and ρ. Starting from this base level, we then fit $R_{0,q,RH,\rho}$ and $R_{Q,0,RH,\rho}$, which represent the effect of image electric forces induced by particles and droplet charges, respectively. The collision rate coefficients vary differently for attractive and repulsive Coulomb forces, so then we fit $R_{Q,q,RH,\rho}$ for opposite sign and same sign charges separately. For the above fitting processes, we separate the particle density into two ranges, $\rho < 1{,}000$ kg m^{-3} and $\rho \geq 1{,}000$ kg m^{-3}, as the weight effects are different for low and high particle densities. We provide graphical results to illustrate the types of variations present and their physical causes and give numerical values of the results in the supporting information for this paper. We have parameterized the results to allow for their use in cloud models, with the parameters and a code to utilize them also in the supporting information.

3. Results

3.1. Collision Rate Coefficients $R_{0,0,RH,\rho}$ and Parameterization for Zero-Charged Droplet and Particles

Figure 4 shows the simulated results of collision rate coefficients $R_{0,0,RH,\rho}$ for zero charges on the droplet and particles, with RH = 95%, 98%, 99%, 100%, and 101% and with particle density ρ = 1, 500, 1,000, 1,500, and 2,000 kg m^{-3}. It is evident that for small particles with radius $a < 0.2$ μm the collision rate coefficient is the same for different particle densities due to the gravitational force being negligible compared with the phoretic forces and diffusion or to electric forces when the particles are charged. Thus, in this paper we only deal with particles with radius $a \geq 0.2$ μm.

In Figure 4 the separation of the families of curves on the left and into the center is due to the variation of the phoretic force. As the weight, fap, and rear collisions increase relative to phoretic effects with increasing particle radius, the curves begin to converge again on the right.

The simulated results for collision rate coefficients in Figure 4 are on a logarithmic scale and suggest that for a given RH and density, the differences between the collision rate coefficients for particles with density of ρ and those with density of 500 kg m^{-3} are very approximately about the same for all values of RH, including RH = 100%, so that the effects of density and RH are roughly independent over most of their ranges, that is

$$R_{0,0,RH,\rho} - R_{0,0,RH,500} \approx R_{0,0,100,\rho} - R_{0,0,100,500} \quad (8)$$

The actual variation of the differences is evidently a slowly varying function of density and phoretic forces and suggests that a useful parameterization for the difference would be in terms of polynomials of the saturation s = (RH − 100), the density difference (ρ − 500), and the particle radius a.

The lower the RH, the stronger the effect of phoretic forces. As shown in Figure 4 for RH = 95% the weight effect is negligible if the particle radius is less than 1.5 μm. We have shown in the previous paper (Zhang & Tinsley, 2017) that for 3 μm radius droplets the phoretic forces reach a maximum at the particle radius of about 1.0 μm. Thus, for larger particles the phoretic forces decrease and the weight increases, so that the weight effect needs to be considered for the large particles even if the RH is less than 95%.

For the simulated results of RH = 100%, as shown by the solid lines in Figure 4, and for particles with density ρ = 1,500 and 2,000 kg m^{-3}, the weight effect tends to increase the collision rate coefficient when the particle radius is large enough to make the fall speed of the particle relative to undisturbed air approach to that of the droplet. This can be seen in Figure 4 as the line for ρ = 2,000 kg m^{-3} crosses the line of ρ = 1,500 kg m^{-3} at the particle radius of about 1.4 μm for RH = 100%. This occurs because for large particles with higher densities the collisions occur at the rear side of droplet, and the process is strongly nonlinear. Also, when the fall speed of particle approaches that of droplet, there is a longer time for the random movement of particles to bring some of them closer to the droplet.

Figure 5 shows the simulated collision rate coefficients for zero charges and RH = 100% as functions of particle density and radius. It can be seen that the rates vary approximately log linearly with particle density when ρ < 1,000 kg m^{-3} and become nonlinear for particle density $\rho \geq$ 1,000 kg m^{-3}. This log linear pattern for particle density ρ < 1,000 kg m^{-3} still holds for RH ≠ 100% (not shown). Figure 5 indicates that the collision rate coefficient varies with particle density in different ways for low and high particle densities, so that for parameterization it will be necessary to fit the collision rate coefficients for particle density less and greater than 1,000 kg m^{-3} separately.

The collision rate coefficients $R_{0,0,\mathrm{RH},\rho}$ will be used as the base level for the further fitting of $R_{Q,q,\mathrm{RH},\rho}$. In order to fit $R_{0,0,\mathrm{RH},\rho}$ with high accuracy, we have calculated the collision rate coefficients for particle densities of ρ = 250, 750, 1,100, 1,250, and 1,750 kg m^{-3}. First, for ρ < 1,000 kg m^{-3}, the collision rate coefficient $R_{0,0,\mathrm{RH},\rho}$ is given in the form of a polynomial in ρ, s, and a by the following expression:

$$R_{0,0,\mathrm{RH},\rho} - R_{0,0,\mathrm{RH},500} = \Sigma_{i,j,k} A_{i,j,k} (\rho - 500)^i s^j a^k \quad (9)$$

where i= 1, 2; j= 0, 1, 2, 3; k= 0, 1, 2; and s = RH − 100 is the saturation.

The values of $R_{0,0,\mathrm{RH},500}$ were obtained from Zhang and Tinsley (2017) using their expressions (1) to (12). The right side of equation (9) represents the summation, for each set of i, j, and k, the product of a coefficient $A_{i,j,k}$, and terms which are the values of ρ, s, and a raised to the powers of i, j, and k, respectively, where the specific values of i, j, and k to be used are given above. The 24 values of the coefficients $A_{i,j,k}$ for the 24 sets of the indices i, j, and k in equation (9) are given in the file, listed as Table S2 under the label "A" in the supporting information. We have given a code "calc_rtcoef.csv" in the file listed as Data Set S1 in the supporting information that can be used to quickly calculate the value of the collision rate coefficient from our parameterization for any value of ρ, s, and a. For use in this code the file "Table S2" in the supporting Information should be re-named "parameter1.txt". Similarly, the file "Text S2" should be re-named "parameter1.txt".

Second, for particle density $\rho \geq$ 1,000 kg m^{-3}, the collision rate coefficients $R_{0,\,0,\,\mathrm{RH},\,\rho}$ are nonlinear and fitted in logarithmic form of another polynomial:

$$\log_{10} R_{0,0,\mathrm{RH},\mathrm{r}} - \log_{10} R_{0,0,\mathrm{RH},500} = \Sigma_{i,j,k} B_{i,j,k} (\rho - 500)^i s^j a^k \quad (10)$$

where i=1, 2, 3, 4, 5;j=0, 1, 2, 3, 4; k=0, 1, 2, 3, 4; and the 125 values of $B_{i,\,j,\,k}$ for the 125 sets of indices can be found in the file parameter2 under the label "B" in the supporting information. As before, and for similar expressions later in this paper, the code calc_rtcoef.csv in the supporting information can be used to quickly obtain desired values of the collision rate coefficient.

With RH decreasing below 95%, the saturation s becomes an increasingly negative value, and the expressions in equations (9) and (10), given in the form of polynomials that include powers of the saturation s, become the sums of large negative and large positive terms, with increasing errors, so that they should not be

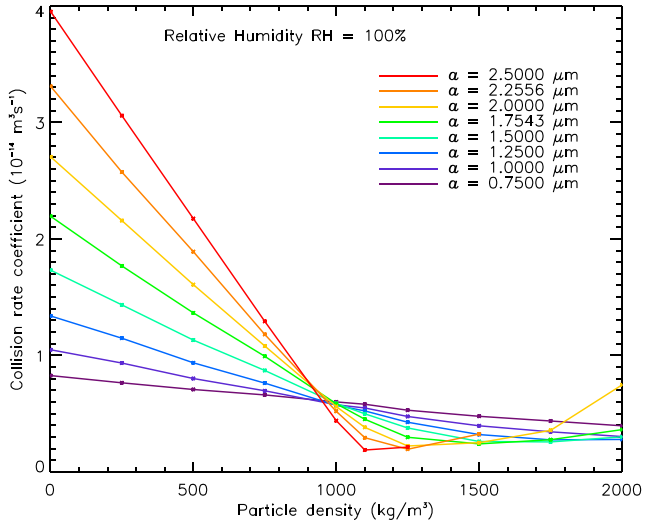

Figure 5. Effects on collision rates of the particle radius and density, in the absence of charges and phoretic effects. Simulated collision rate coefficients $R_{0,0,100\%,\rho}$ for a wide range of particle densities ρ and particle radii a. On the left the rate coefficients for particle densities less than 1,000 kg m^{-3} vary log linearly with particle radius and particle density. On the right, with $\rho >$ 1,000 kg m^{-3} and increasing particle radii, the rates reflect increasingly nonlinear interactions of weight, flow around the particle, and rear collisions as the fall speed of the particle approaches that of the droplet.

used to estimate the collision rate coefficient in this case. However, if the RH $<$ 95%, equation (8) is a better approximation for $R_{0,0,RH,\rho}$, and from the trends in Figure 4 it can be seen that if RH $\ll$95%, the weight effect is negligible and we have $R_{0,0,RH,\rho} \approx R_{0,0,RH,500}$.

3.2. Collision Rate Coefficients $R_{0,\,q,\,RH,\,\rho}$ and Parameterizations for Charged Particles and Uncharged Droplets

With particle charge $q \neq 0e$, the image electric force induced by particles tends to increase the collision rate coefficient, and this effect is more significant for small particles due to their high mobility. Figure 6 shows the collision rate coefficient $R_{0,\,q,\,RH,\,\rho}$ for RH = 100%, with zero droplet charge; particle charge q = 0e, 10e, 20e, 50e, and 100e; and particle density ρ = 1, 500, 1,000, 1,500, and 2,000 kg m^{-3}. The effect of image electric force dominates for small particles with radius less than 0.2 μm, while intercept, fap, and weight effects become significant for larger particles.

For particle densities $\rho \geq$ 1,000 kg m^{-3}, the effect of the image electric force decreases for large particles. This is because the stagnation region prevents particles from moving close to the droplet as in Figures 1 and 2, which limits the range for the short-range image electric force, and hence, its effect on the collision rate coefficient for heavy particles is weaker. At the particle radius for which the fall speed $U_{a,\,\infty}$ of the particle equals $U_{A,\,\infty}$, the fall speed of the droplet, the rate coefficient vanishes because the approach to the droplet does not begin.

For particle density $\rho <$ 1,000 kg m^{-3}, the collision rate coefficient can be approximately estimated by

$$R_{0,q,RH,\rho} \approx R_{0,q,RH,500} + R_{0,0,RH,\rho} - R_{0,0,RH,500} \tag{11}$$

The values of $R_{0,q,RH,500}$ simulated by Zhang and Tinsley (2017) have been supplemented with some new simulations of greater accuracy. For the present work new parameterizations of $R_{0,q,RH,500}$ in accordance with the equations (17) and (18) of Zhang and Tinsley (2017) are given in the file (for use as parameter1.txt), listed as Text S2 of the supporting information, under the label "B1" for $a \leq$ 0.2 μm with RH $<$ 100%, the label "B2" for $a \leq$ 0.2 μm with RH $\geq$ 100%, the label "C1" for $a \geq$ 0.2 μm with RH $<$ 100%, and the label "C2" for $a \geq$ 0.2 μm with RH $\geq$ 100%.

Figure 7 compares the two sides of equation (11) for RH = 100%, with the small squares being the simulated results of collision rate coefficient $R_{0,\,q,\,RH,\,\rho}$ and the lines being the results of $R_{0,\,0,\,RH,\,\rho}$+ $R_{0,\,q,\,RH,\,500}$− $R_{0,\,0,\,RH,\,500}$. It is clear that the two sides of equation (11) match well over most of the range. For the case of particle charge q = 100e and droplet density ρ = 1,000 kg m^{-3}, the collision rate coefficients are overestimated by about 10% as shown in Figure 7; this is because the effects of image electric force and weight are both strong, and the collision rate coefficient is not accurately estimated by the sum of the two effects. In addition, for the cases of RH ≠ 100% which are not shown, equation (11) still holds well. In the right side of equation (11) the term $R_{0,0,RH,\rho} - R_{0,0,RH,500}$ changes roughly linearly with particle density for $\rho <$ 1,000 kg m^{-3}, and as shown in Figure 5, the collision rate coefficients $R_{0,q,RH,\rho}$ are also approximately linear with particle density for $\rho <$ 1,000 kg m^{-3}.

For particle density $\rho <$ 1,000 kg m^{-3}, we make a more accurate fit for $R_{0,q,RH,\rho}$ in the form

$$R_{0,q,RH,\rho} - R_{0,q,RH,500} - R_{0,0,RH,\rho} + R_{0,0,RH,500} = \Sigma_{i,j,k,r} C_{i,j,k,r} (\rho - 500)^i |q|^j s^k a^r \tag{12}$$

where i = 1, 2; j = 1, 2; k = 0, 1, 2, 3; r = 0, 1, 2, 3; and the 64 values of $C_{i,\,j,\,k,\,r}$ can be found in the file parameter2 under the label "C" in the supporting information.

As the left side in equation (12) is equal to zero if ρ = 500 kg m^{-3} or q = 0e, the values of "i" and "j" start from 1 rather than from 0. With RH $<$ 95% or particle charge $q >$ 100e, we can apply equation (11) to estimate the collision rate coefficient.

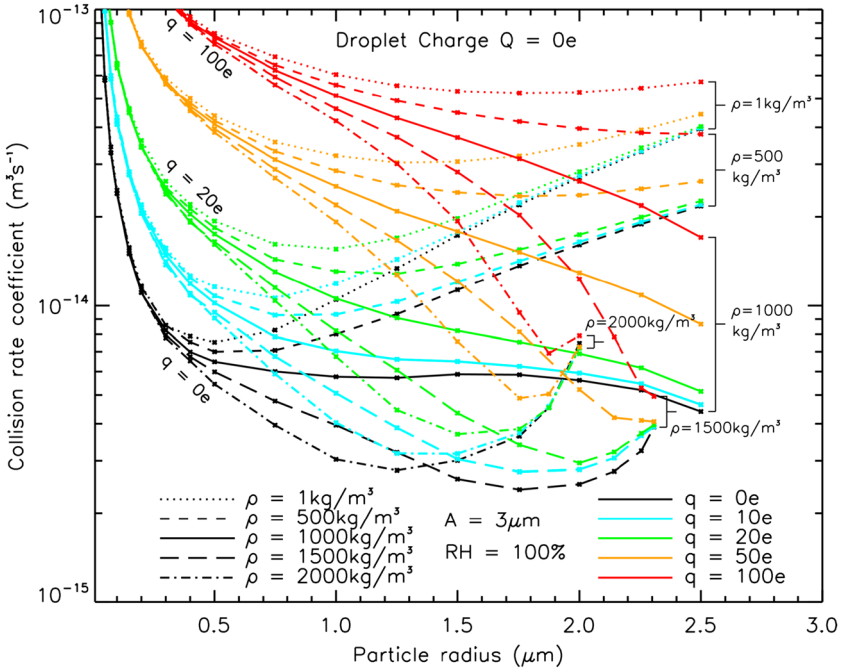

Figure 6. Effects of density and particle charges. Simulated collision rate coefficients, $R_{0,q,100\%,\rho}$, with particle charge q = 0*e*, 10*e*, 20*e*, 50*e*, and 100*e* and particle density ρ = 1, 500, 1,000, 1,500, and 2,000 kg m^{-3}. The separation of the families of curves on the left is due to the image attractive forces increasing with particle charge. The separation in the center within charge families is due to increased flow around the particle, weight, and rear collisions. There is a convergence as a function of density on the right, and for density of 1,500 and 2,000 kg m^{-3} the curves terminate when the particle fall speed is the same as the droplet fall speed.

For particle density $\rho \geq$ 1,000 kg m^{-3}, we fit $R_{0,q,\mathrm{RH},\rho}$ more accurately in the form:

$$\log_{10}R_{0,q,RH,\rho} - \log_{10}R_{0,q,\mathrm{RH},500} - \log_{10}R_{0,0,\mathrm{RH},\rho} + \log_{10}R_{0,0,\mathrm{RH},500} = \Sigma_{i,j,k,r}D_{i,j,k,r}(\rho - 500)^i|q|^j s^k a^r \quad (13)$$

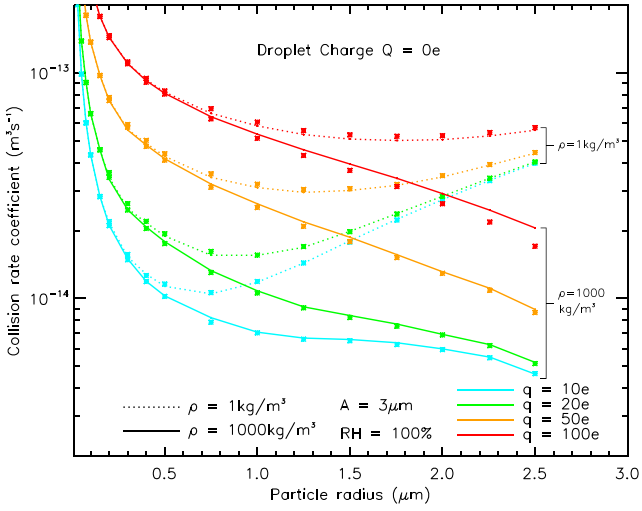

Figure 7. Comparison of simulations and approximate fitting for effects of particle charges. Small squares are simulated results of collision rate coefficient $R_{0,q,100\%,\rho}$, and lines are the result for $R_{0,0,100\%,\rho} + R_{0,q,100\%,500} - R_{0,0,100\%,500}$; for particle charge q = 10*e*, 20*e*, 50*e*, and 100*e*; and particle density ρ = 1 and 1,000 kg m^{-3}. The agreement is good over most of the range, but the approximate fit (line) overestimates the rates by about 10% for q = 100*e*.

where i = 1, 2, 3; j = 1, 2, 3; k = 0, 1, 2, 3, 4; r = 0, 1, 2, 3, 4; and the 225 values of $D_{i,j,k,r}$ can be found in the file parameter2 under the label "D" in the supporting information. With the RH < 95%, the attractive phoretic forces are strong and the collision rate coefficient can be estimated as $R_{0,0,\mathrm{RH},\rho} \approx R_{0,q,\mathrm{RH},1000}$, for which the value of $R_{0,q,\mathrm{RH},1000}$ can be calculated by equation (11).

3.3. Collision Rate Coefficients $R_{Q,0,\mathrm{RH},\rho}$ and Parameterization for Charged Droplets and Uncharged Particles

With droplet charge $Q \neq 0e$ the droplet can induce an image electric force on large particles, irrespective of the charge on the particle. Figure 8 shows, for particle charge q = 0 and RH = 100%, the collision rate coefficient $R_{Q,0,\mathrm{RH},\rho}$ for droplet charge Q = 0*e*, 10*e*, 20*e*, 50*e*, and 100*e* and particle density ρ = 1, 500, 1,000, 1,500, and 2,000 kg m^{-3}, in which the effect of image electric force is negligible for small particles and increases with droplet charge. The curves separate in the middle of the figure because of greater weight effects and greater image charge forces for the larger particles. The collision rate coefficients $R_{Q,0,\mathrm{RH},\rho}$ for different droplet charges converge for particle density 1,500 and 2,000 kg m^{-3}, as for the collision rate coefficient $R_{0,q,\mathrm{RH},\rho}$ in Figure 6. The reason is also that the stagnation region prevents particles from moving close to the droplet, so the effect of the short-range droplet

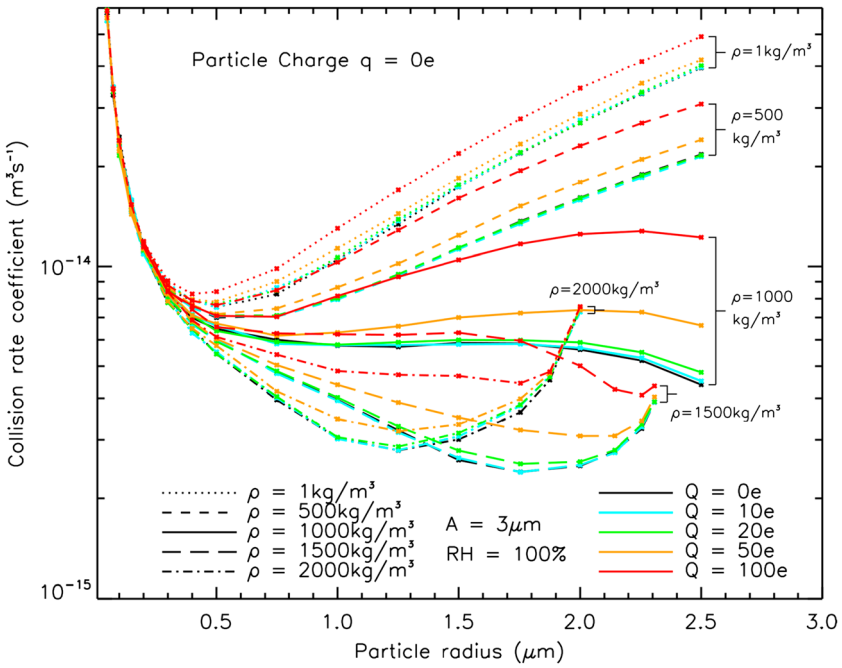

Figure 8. Effects of density and droplet charges. Simulated results of collision rate coefficient $R_{Q,0,100\%,\rho}$ for droplet charge Q = 0*e*, 10*e*, 20*e*, 50*e*, and 100*e* and particle density ρ = 1, 500, 1,000, 1,500, and 2,000 kg m^{-3}. The curve separates in the middle range of particle radii, due to the droplet image attractive force increasing with particle radii for a given droplet charge. As in Figure 6, the amount of convergence of curves to the right increases with increasing density, and the curves terminate at the radius where the particle fall speed equals that of the droplet.

image electric force on the collision rate coefficient is increasingly limited as the fall speed of the particle in the undisturbed air approaches that of the droplet. As in Figure 6 the curves for ρ = 1,500 and 2,000 kg m^{-3} terminate when the fall speeds are equal.

For particle density ρ < 1,000 kg m^{-3} the collision rate coefficient can be approximately estimated by

$$R_{Q,0,\mathrm{RH},\rho} \approx R_{0,0,\mathrm{RH},\rho} + R_{Q,0,\mathrm{RH},500} - R_{0,0,\mathrm{RH},500} \tag{14}$$

The variation of $R_{Q,0,\mathrm{RH},\rho}$ with RH and Q is shown in Figure 9 as small squares, together with the lines which are the variation of the right side of equation (14).

It is apparent that equation (14) is a good approximation to the collision rate coefficient over most of the range; however, for RH = 101% the approximation overestimates the collision rate coefficient a little for droplet charge Q = 50*e* and 100*e* and particle density ρ = 1,000 kg m^{-3}, as the total effects of attractive image force, repulsive phoretic forces, and gravitational force are not accurately estimated by the sum of each effect.

The very low collision rates for RH = 101% result from the repulsive phoretic force negating diffusion, and the increase due to the droplet image charge Q = 100*e* is about a factor of 4 at $a \approx 2$ μm. A similar effect was found for particle image charge (Zhang & Tinsley, 2017, Figure 6), where for q = 10*e* there was a factor of 3 increase at $a \approx 0.5$ μm, and for q = 20*e* there was a factor of 12 increase.

For particle density $\rho \leq$ 1,000 kg m^{-3}, we fit $R_{Q,0,\mathrm{RH},\rho}$ more accurately in the form

$$R_{Q,0,\mathrm{RH},\rho} - R_{Q,0,\mathrm{RH},500} - R_{0,0,\mathrm{RH},\rho} + R_{0,0,\mathrm{RH},500} = \Sigma_{i,j,k,r} E_{i,j,k,r} (\rho - 500)^i |Q|^j s^k a^r \tag{15}$$

where i = 1, 2; j = 1, 2; k = 0, 1, 2, 3; and r = 0, 1, 2, 3. A new parameterization of $R_{Q,0,\mathrm{RH},500}$ in accordance with Zhang and Tinsley (2017, equation 21) is given in the file parameter1 under the label "D" for $a \geq 0.5$ μm. For $a < 0.5$ μm there is negligible effect of droplet image charge, and $R_{Q,0,\mathrm{RH},500} = R_{0,0,\mathrm{RH},500}$. The 64 values of $E_{i,j,k,r}$ can be found in the file parameter2 under the label "E" in the supporting information. As the left side in equation (15) is equal to zero if ρ = 500 kg m^{-3} or q = 0*e*, the values of i and j in the right side start from 1 rather than 0. With RH < 95% or droplet charge Q > 100*e* the

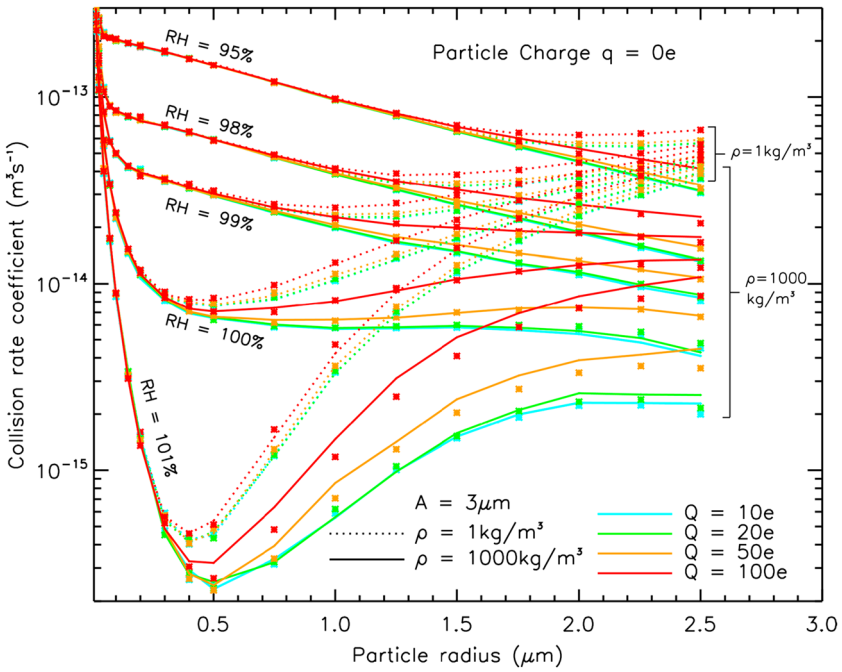

Figure 9. Comparison of simulations and approximate fitting for effects of droplet charges Q. Small squares are the simulated collision rate coefficients $R_{Q,0,\mathrm{RH},\rho}$ and lines are the results of $R_{0,0,\mathrm{RH},\rho} + R_{Q,0,\mathrm{RH},500} - R_{0,0,\mathrm{RH},500}$, for $Q = 10e$, $20e$, $50e$, and $100e$; RH = 95%, 98%, 99%, 100%, and 101%; and particle density ρ = 1 and 1,000 kg m^{-3}. The agreement with this approximate formula is good except for particle charges of $50e$ and $100e$ for RH = 101%. The very low collision rates for RH = 101% result from the repulsive phoretic forces negating diffusion. The increase due to the droplet image charge for RH = 101% is about a factor of 4 at $a \approx 2$ μm.

polynomial $|Q|^j s^k$ in equation (15) may diverge, then equation (14) is a good alternative to estimate the collision rate coefficient.

For particle density $\rho \geq 1{,}000$ kg m^{-3}, we fit $R_{Q,0,\mathrm{RH},\rho}$ in the form

$$\log_{10}R_{Q,0,RH,\rho} - \log_{10}R_{Q,0,\mathrm{RH},500} - \log_{10}R_{0,0,\mathrm{RH},\rho} + \log_{10}R_{0,0,\mathrm{RH},500} = \Sigma_{i,j,k,r}F_{i,j,k,r}(\rho - 500)^i|Q|^j s^k a^r \quad (16)$$

where i = 1, 2, 3; j = 1, 2, 3; k = 0, 1, 2, 3, 4; and r = 0, 1, 2, 3, 4 and 225 values of $F_{i,j,k,r}$ can be found in the file parameter2 under the label "F" in the supporting information. When the RH $<$ 95%, the attractive phoretic forces are strong and the collision rate coefficient can be estimated as $R_{Q,0,\mathrm{RH},\rho} \approx R_{Q,0,\mathrm{RH},1000}$ for which the value of $R_{Q,0,\mathrm{RH},1000}$ can be calculated by equation (14).

3.4. Collision Rate Coefficients $R_{Q,q,\mathrm{RH},\rho}$ and Parameterization for Opposite Sign Droplet Charge and Particle Charge

Figure 10 shows the collision rate coefficients for RH = 100%, particle charge $q = 10e$, droplet charge $Q = 0e$, $-10e$, $-20e$, $-50e$, and $-100e$ and particle density ρ = 1, 500, 1,000, 1,500, and 2,000 kg m^{-3}. The separation of the families of curves of a given droplet charge for $a < 1$ μm is due to the combined Coulomb and particle image attractive forces. With increasing weight the separation within charge families leads to convergence as a function of density at the larger particle radii, together with the effects of increasing fap and rear collisions. The density families terminate when the particle fall speed equals that of the droplet.

For particle densityρ<1,000 kg m^{-3}, the effects of Coulomb forces for opposite sign droplet and particle charges are approximately independent of the weight effect, and a good estimation of collision rate coefficient is given as

$$R_{Q,q,\mathrm{RH},\rho} \approx R_{0,q,\mathrm{RH},\rho} + R_{Q,q,\mathrm{RH},500} - R_{0,q,\mathrm{RH},500} \quad (17)$$

Figure 11 compares the two sides of equation (17) for RH = 100%, particle charge $q = 10e$, and particle densities ρ = 1 and 1,000 kg m^{-3}. The small squares represent the simulated results of collision rate

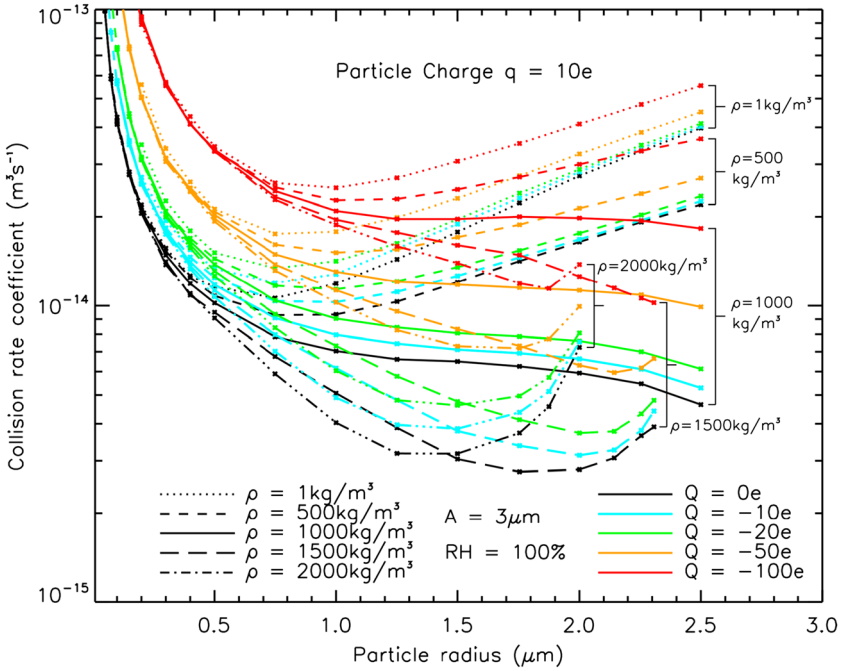

Figure 10. Effects of density of particles on collision rate coefficients $R_{Q,q,100\%,\rho}$ for opposite sign droplet and particle charges. The droplet charges are $Q = 0e$, $-10e$, $-20e$, $-50e$, and $-100e$; and particle densities are $\rho = 1$, 500, 1,000, 1,500, and 2,000 kg m^{-3}. The separation of curves for charge families beginning on the left is due to the attractive Coulomb force, with droplet image charge attractive force increasing toward the right. The separation as a function of density in the center and convergence toward the right for larger densities and increasing radii are due to increasing weight, flow around the particle, and rear collisions as particle fall speeds approach that of the droplet.

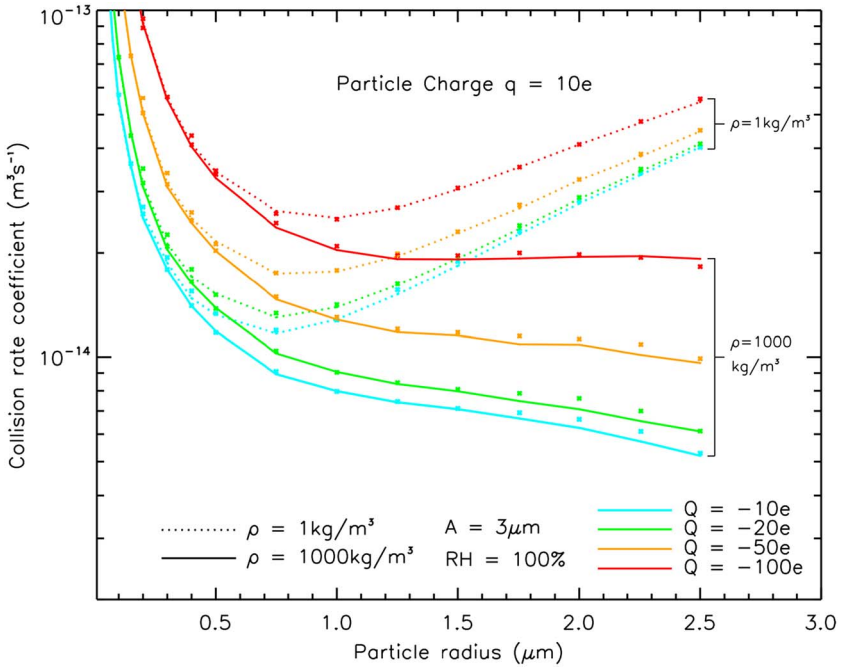

Figure 11. Comparison of simulations and approximate fitting for effects of opposite sign particle and droplet charges. Small squares are the simulated result of collision rate coefficient $R_{Q,q,100\%,\rho}$; lines are the results of $R_{0,q,100\%,\rho} + R_{Q,q,100\%,500} - R_{0,q,100\%,500}$ for droplet charges $Q = -10e$, $-20e$, $-50e$, and $-100e$ and particle densities $\rho = 1$ and 1,000 kg m^{-3}. For this lower range of particle densities this approximation fits the simulations reasonably well.

coefficient and the lines representing the result of $R_{0,q,\mathrm{RH},\rho} + R_{Q,q,\mathrm{RH},\ 500} - R_{0,q,\mathrm{RH},500}$. It is evident that equation (17) fits the simulation well for this lower range of particle densities. Also (not shown), for RH = 95%, 98%, 99%, and 101% and particle charge q = 20e and 50e, equation (17) is also quite valid. For particle density $\rho \geq$ 1,000 kg m^{-3}, equation (17) is still applicable for small particles but is only a poor estimate of the collision rate coefficient for large particles. Unlike Figures 6 and 8, in which the collision rate coefficients of $\rho \geq$ 1,000 kg m^{-3} for different charges tend to converge at the particle radius where the fall speed of particles in quiet air is equal to that of the droplet, the collision rate coefficients in Figure 11 do not converge at large particle radius. This is because the long-range Coulomb force acts earlier in the trajectory and its effect is not strongly influenced by the presence of the stagnation region near the droplet.

For particle density $\rho <$ 1,000 kg m^{-3}, we fit the collision rate coefficient more accurately as follows:

$$\begin{aligned}&\left(R_{Q,q,\mathrm{RH},\rho} - R_{0,q,\mathrm{RH},\rho} - R_{Q,0,\mathrm{RH},\rho} + R_{0,0,\mathrm{RH},\rho}\right) - \left(R_{Q,q,\mathrm{RH},500} - R_{0,q,\mathrm{RH},500} - R_{Q,0,\mathrm{RH},500} + R_{0,0,\mathrm{RH},500}\right)\\ &\quad = \Sigma_{i,j,k,r,t} G_{i,j,k,r,t} (\rho - 500)^i |Q|^j |q|^k s^r a^t \end{aligned} \tag{18}$$

where i = 1, 2; j = 1, 2; k = 1, 2; r = 0, 1, 2, 3; and t = 0, 1, 2, 3. For $R_{Q,q,\mathrm{RH},500}$ a new parameterization for $a <$ 0.2 μm in accordance with equations (23) and (24) of Zhang and Tinsley (2017) is given in the file parameter1 of the supporting information, under the label "F". The parameterization for $a \geq$ 0.2 μm in accordance with equations (25) and (26) of Zhang and Tinsley (2017) is given in the file parameter1 of the supporting information, under the label "H." The 128 values of $G_{i,j,k,r,t}$ can be found in the file parameter2 under the label "G" in the supporting information. When Q = 0e or q = 0e or ρ = 500 kg m^{-3}, the left side is equal to zero, so that i, j, and k start from 1 rather than 0.

For particle density $\rho \geq$ 1,000 kg m^{-3}, the collision rate coefficients vary differently from those for particle density ρ = 500 kg m^{-3}, so that we fit the collision rate coefficient in the following way:

$$\log_{10}\left(R_{Q,q,RH,\rho} - R_{0,q,\mathrm{RH},\rho}\right) - \log_{10}\left(R_{Q,q,\mathrm{RH},500} - R_{0,q,\mathrm{RH},500}\right) = \Sigma_{i,j,k,r,t} H_{i,j,k,r,t} (\rho - 500)^i |Q|^j |q|^k s^r a^t \tag{19}$$

where i = 1, 2, 3; j = 0, 1, 2; k = 0, 1, 2; r = 0, 1, 2, 3; and t = 0, 1, 2, 3, 4 and the 540 values of $H_{i,j,k,r,t}$ can be found in the file parameter2 under the label "H" in the supporting information.

3.5. Collision Rate Coefficients $R_{Q,q,\mathrm{RH},\rho}$ and Parameterization for Same Sign Droplet Charge and Particle Charge

Figure 12 shows the collision rate coefficient $R_{Q,q,\mathrm{RH},\rho}$ for RH = 100%; particle charge q = 10e; particle charge Q = 0e, 10e, 20e, 50e, and 100e; and particle density ρ = 1, 500, 1,000, 1,500, and 2,000 kg m^{-3}. The collision rate coefficients for large particle radii are strongly affected by particle density, because the repulsive Coulomb force for the same sign charges acts in opposition to the effects of attractive forces and diffusion. For particle charge q = 20e and 50e (not shown) the Coulomb repulsion is even greater as are the effects of particle density. The decrease in rate coefficient for droplet charges 50e and 100e for $a <$ 0.5 μm is because for small particles the long-range Coulomb repulsion force has a greater effect than the short-range image attractive forces. With increasing particle radii the separation within charge families as a function of density is reduced, leading to convergence for specific densities at large particle radii. Again, the terminations of the curves, at increased rate coefficients, for ρ = 1,500 and 2,000 kg m^{-3}, are due to the increasing weight, fap, and rear collisions as the fall speeds of the particles approach that of the droplet.

For RH ≤ 95% (not shown), and in contrast to the case for opposite sign charges on droplets and particles, where the weight effect is small or even negligible compared with the electric and phoretic effects, the weight effect is still considerable.

In Figure 12, for particle density $\rho <$ 1,000 kg m^{-3} with RH = 100%, when the particle radius $a \geq$ 2.0 μm, the collision rate coefficient $R_{Q,q,\mathrm{RH},\rho}$ for large droplet charges can be greater than that for small droplet charges. For example $R_{100,10,100\%,1000} > R_{10,10,100\%,1000}$. This is because the image electric force induced by the droplet charges becomes greater on larger particles. This phenomenon disappears for particle density $\rho \geq$ 1,000 kg m^{-3}, because, with particles less able to enter the stagnation region near the droplet, the effects of the long-range Coulomb force dominate over those of the short-range image electric force.

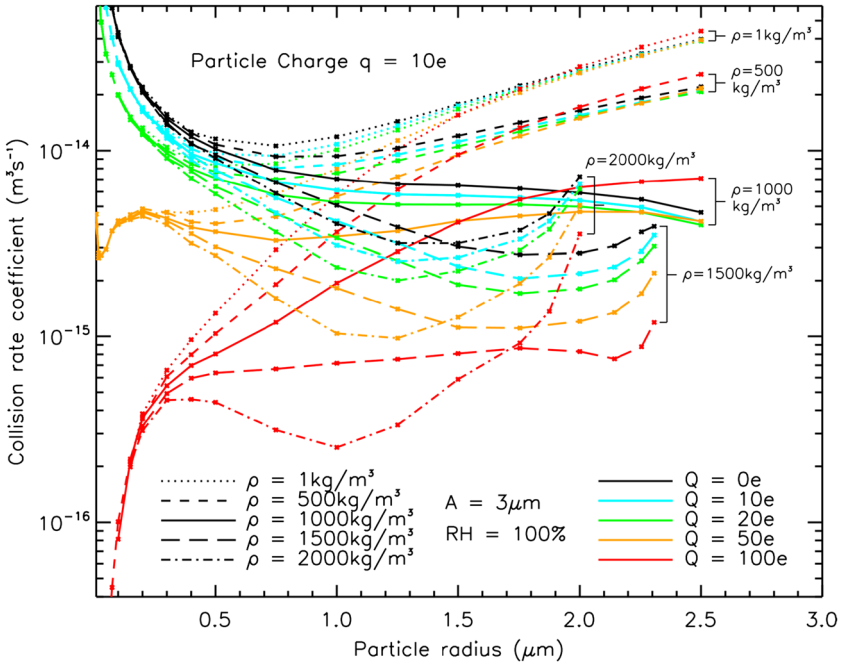

Figure 12. Effects of density on collision rate coefficients $R_{Q,q,100\%,\rho}$ for same sign droplet and particle charges. Results for droplet charges Q = 0*e*, 10*e*, 20*e*, 50*e*, and 100*e* and particle density ρ = 1, 500, 1,000, 1,500, and 2,000 kg m^{-3}. Here the separation of charge family curves on the left is due to the stronger Coulomb repulsion than particle image attraction forces. The separation within the charge families in the center and convergence toward the right as a function of density are due to the increasing weight, flow around the particle, and rear collisions.

When the droplet and particle charges are same sign, the range of collision rate coefficients is very wide, so that they are fitted in the logarithmic mode for the full range of ρ as follows:

$$\log_{10}R_{Q,q,RH,\rho} - \log_{10}R_{0,q,RH,\rho} - \log_{10}R_{Q,q,RH,500} + \log_{10}R_{Q,q,RH,500} = \Sigma_{i,j,k,r,t}U_{i,j,k,r,t}(\rho - 500)^i|Q|^j|q|^k s^r a^t \quad (20)$$

where i = 1, 2, 3, 4; j = 1, 2; k = 1, 2; r = 0, 1, 2, 3, 4; and t = 0, 1, 2, 3, 4, 5. For $R_{Q,q,RH,500}$ a new parameterization for $a < 0.2$ μm in accordance with equations (29) and (30) of Zhang and Tinsley (2017) is given in the file parameter1 of the supporting information, under the label "M." The parameterization for $a \geq 0.2$ μm in accordance with equations (31) and (32) of Zhang and Tinsley (2017) is given in the file parameter1 of the supporting information, under the label "V." The 480 values of $U_{i,j,k,r,t}$ can be found in the file parameter2 under the label "U" in the supporting information.

4. Discussion and Conclusion

Simulations and parameterization of collision rate coefficients for 3 μm radius droplets have been extended to a wide range of particle densities. For small particles with radius less than 0.2 μm the weight effect can be neglected, while it becomes significant for greater particles. In this paper, we only calculate and parameterize the collision rate coefficient for particle radii $a \geq 0.2$ μm to investigate the weight effect.

For particle density $\rho \geq$ 1,000 kg m^{-3}, the weight of the particles tends to pull them away from the droplet and thus reduces the collision rate coefficient. The collision rate coefficients vary approximately linearly with particle density in the absence of phoretic forces and electric forces for particle density $\rho <$ 1,000 kg m^{-3}. Also, the weight effect is roughly independent of the effects of other forces, and the collision rate coefficients can be obtained approximately by the sum of each effect if the other forces are not strongly repulsive. If the RH is very low, the effect of phoretic forces can predominate over the weight effect and then the weight effect can be neglected.

For particle density $\rho \geq$ 1,000 kg m^{-3}, the effect of the stagnation region ahead of the droplet in conjunction with the particle's weight becomes significant and results in complex effects. First, the stagnation region can

prevent the collision occurring at the front side of the droplet while diverting particles for collisions at its rear. When the fall speed of the particle relative to undisturbed air approaches that of the droplet, more time is available for particles released below to pass near the droplet. Thus, diffusion can transport more particles behind the droplet to the region through which particles can fall and collide with the rear of the droplet. Thus, in this condition the weight effect tends to increase rather than decrease the collision rate coefficient. Second, the tendency for the particles to be excluded from the stagnation region prevents the short-range image electric forces acting, while it has little influence on the effects of the long-range Coulomb forces. Thus, when the fall speed of particle relative to undisturbed air approaches to that of droplet, the effect of short-range image electric forces is negligible. For particles with density $\rho \geq 1{,}000$ kg m^{-3}, the image electric forces can be more significant than the Coulomb force and enhance the process of scavenging even if droplet and particles have the same sign charge. However, for large particles with density $\rho \geq 1{,}000$ kg m^{-3} with the same sign charge as droplet, the effects of image electric forces are reduced and the repulsive Coulomb force is predominant.

The parameterization can be applied with caution outside the temperature and pressure values of 540 hPa and 256 K. Changes in the rate coefficients with altitude can be estimated from Figure 8 in Tinsley and Leddon (2013). Going down from 540 hPa to the surface or up to 300 hPa, the rates change by less than 20%.

In brief, the collision rate coefficients become very complex when the weight effect is included in conjunction with diffusion, electric forces, phoretic forces, intercept effect, and fap. We have parameterized the simulated results of the collision rate coefficients to make it easy for them to be applied in cloud models and compared with observations, such as discussed in the section "Atmospheric Relevance." In previous comparisons with field experiments of below-cloud scavenging (e.g., Andronache et al., 2006; Davenport & Peters, 1978; Wang et al., 2010) the measured scavenging rates were found to be considerably greater than modeled. This could partly be due to the neglect of image charges in the previous modeling, contributions from in-cloud scavenging in air advected downward, other electrical and nonelectrical microphysical processes, and errors in the models discussed in section 2.1, which substantially underestimate the collision rates. There is a need for improved field measurements to compare with accurate models, for both below-cloud and in-cloud scavenging, to resolve this.

For using the parameterized results, we have provided in the supporting information a file labeled Text S2 parameters fitted to slightly more accurate simulations for density 500 kg m^{-3} than in the previous paper (Zhang & Tinsley, 2017). The files labeled Table S2 are for particle densities other than 500 kg m^{-3}. The file of Data Set S1 provides the code written in IDL to reconstruct the collision rate coefficients as required. We have provided several approximate equations which could be useful in restricted applications.

In summary, we have obtained and parameterized collision rate coefficients $R_{Q,q,A,a,\mathrm{RH},\rho}$ for droplet radius A = 3.0 μm and for a realistic set of droplet charges Q, particle charges q, particle radii a, relative humidities RH, and particle densities ρ. We plan to complete the calculation and parameterization of collision rate coefficients for greater droplet radii as a function of particle density in future work, so that, together with previous work, the collision rate coefficients $R_{Q,q,A,a,\mathrm{RH},\rho}$ can be readily obtained for all needed cases and applied in cloud models.

Acknowledgments
This work has been funded by NSF grant AGS 0855351, UTD internal funds, and NSFC (41571040). The numerical values of the simulations are given in Table S1 (supplementary.xsl) in the supporting information. Also given are the numerical values of the parameterization, which can be used with the IDL code (labeled Data Set S1 (calc_rtcoef.csv).

References

Abbas, M. A., & Latham, J. (1969). The electrofreezing of supercooled water drops. *Journal of the Meteorological Society of Japan*, *47*, 65–74.

Andronache, C., Grönholm, T., Laasko, L., Phillips, V., & Venäläinen, A. (2006). Scavenging of ultrafine particles by rainfall at a boreal site: Observations and model simulations. *Atmospheric Chemistry and Physics*, *6*, 4739–4754.

Burns, G. B., Tinsley, B. A., French, W. J. R., Troshichev, O. A., & Frank Kamenetsky, A. V. (2008). Atmospheric circuit influences on ground-level pressure in the Antarctic and Arctic. *Journal of Geophysical Research*, *113*, D15112. https://doi.org/10.1029/2007JD009618

Davenport, H. M., & Peters, L. K. (1978). Field studies of atmospheric particulate concentration changes during precipitation. *Atmospheric Environment*, *12*, 997–1008.

Davis, M. H. (1964a). *Two charged spherical conductors in a uniform electric field: Forces and field strength, RM-3860-PR* (p. 35). Santa Monica, CA: The Rand Corp.

Davis, M. H. (1964b). Two charged spherical conductors in a uniform electric field: Forces and field strength. *Quarterly Journal of Mechanics and Applied Mathematics*, *17*, 400–511.

Frank-Kamenetsky, A. V., Kotikov, A. L., Kruglov, A. A., Burns, G. B., Kliemenova, N. G., Kozyreva, O. V., … Odzimek, A. (2012). Variations in the near-surface atmospheric electric field at high latitudes and ionospheric potential during geomagnetic perturbations. *Geomagnetism and Aeronomy*, *52*(5), 629–638. https://doi.org/10.1134/S0016793212050064

Frederick, J. E. (2016). Solar irradiance observed at Summit, Greenland: Possible links to magnetic activity on short timescales. *Journal of Atmospheric and Solar - Terrestrial Physics*, *147*, 59–70. https://doi.org/10.1016/j.jastp.2016.07.001

Frederick, J. E. (2017). An analysis of couplings between solar activity and atmospheric opacity at the South Pole. *Journal of Atmospheric and Solar - Terrestrial Physics*, *164*, 97–104. https://doi.org/10.1016/j.jastp.2017.08.011

Hand, J. L., & Kreidenweis, S. M. (2002). A new method for retrieving particle refractive index and effective density from aerosol size distribution data. *Aerosol Science and Technology*, *36*(10), 1012–1026. https://doi.org/10.1080/02786820290092276

Khain, A., Arkhipov, V., Pinsky, M., Feldman, Y., & Ryabov, Y. (2004). Rain enhancement and fog elimination by seeding with charged droplets. Part I: Theory and numerical simulations. *Journal of Applied Meteorology*, *43*, 1513–1529.

Kniveton, D. R., Tinsley, B. A., Burns, G. B., Bering, E. A., & Troshichev, O. A. (2008). Variations in global cloud cover and the fair-weather vertical electric field. *Journal of Atmospheric and Solar - Terrestrial Physics*, *70*, 1633–1642.

Ladino, L. A., Stetzer, O., & Lohman, U. (2013). Contact freezing: A review of experimental studies. *Atmospheric Chemistry and Physics*, *13*, 9745–9769. https://doi.org/10.5194/acp-13-9745-2013

Lam, M. M., Chisham, G., & Freeman, M. P. (2013). The interplanetary magnetic field influences mid-latitude surface atmospheric pressure. *Environmental Research Letters*, *8*, 045001. https://doi.org/10.1088/1748-9326/8/4/045001

Lam, M. M., Chisham, G., & Freeman, M. P. (2014). Solar-wind-driven geopotential height anomalies originate in the Antarctic lower troposphere. *Geophysical Research Letters*, *41*, 6509–6514. https://doi.org/10.1002/2014GL061421

Lam, M. M., Freeman, M. P., & Chisham, G. (2017). IMF-driven change to the Antarctic tropospheric temperature due to global atmospheric electric circuit. *Journal of Atmospheric and Solar - Terrestrial Physics*. https://doi.org/10.1016/j.jastp.2017.08.027

Langmuir, L. (1948). The production of rain by a chain reaction in cumulus clouds at temperatures above freezing. *Journal of Meteorology*, *5*, 175–192.

Nicoll, K. A., & Harrison, R. G. (2016). Stratiform cloud electrification: Comparison of theory with multiple in-cloud measurements. *Quarterly Journal of the Royal Meteorological Society*, *142*, 2679–2691. https://doi.org/10.1002/qj.2858

Pruppacher, H. R., & Klett, J. D. (1997). *Microphysics of clouds and precipitation* (2nd ed., p. 954). New York: Springer.

Rosenfeld, D., Kaufman, Y. K., & Koren, I. (2006). Switching cloud cover and dynamical regimes from open to closed Bernal cells in response to suppression of precipitation by aerosols. *Atmospheric Chemistry and Physics*, *6*, 2503–2511.

Rosenfeld, D., Lohmann, U., Raga, G. B., O'Dowd, C. D., Kulmala, M., Fuzzi, S., … Andreae, M. O. (2008). Flood or drought: How do aerosols affect precipitation? *Science*, *321*(5894), 1309–1313. https://doi.org/10.1126/science.1160606

Tinsley, B. A. (2010). Electric charge modulation of aerosol scavenging in clouds: Rate coefficients with Monte Carlo simulation of diffusion. *Journal of Geophysical Research*, *115*, D23211. https://doi.org/10.1029/2010JD014580

Tinsley, B. A. (2012). A working hypothesis for connections between electrically-induced charges in cloud microphysics and storm vorticity, with possible effects on circulation. *Advances in Space Research*, *50*(2012), 791–805.

Tinsley, B. A., & Dean, G. W. (1991). Apparent tropospheric response to MeV-GeV particle flux variations: A connection via electrofreezing of supercooled water in high-level clouds? *Journal of Geophysical Research*, *96*(D12), 22,283–22,296.

Tinsley, B. A., & Leddon, D. (2013). Charge modulation of scavenging in clouds: Extension of Monte-Carlo simulations and initial parameterization. *Journal of Geophysical Research*, *118*, 8612–8624. https://doi.org/10.1002/jgrd.50618

Tinsley, B. A., & Yu, F. (2004). Atmospheric ionization and clouds as links between solar activity and climate. In J. Pap & P. Fox (Eds.), *Solar variability and its effects on climate*, *Geophysical Monograph Series* (Vol. 141, pp. 321–339). Washington, DC: American Geophysical Union.

Tinsley, B. A., & Zhou, L. (2015). Parameterization of aerosol scavenging due to atmospheric ionization. *Journal of Geophysical Research: Atmospheres*, *120*, 8389–8410. https://doi.org/10.1002/2014JD023016

Tinsley, B. A., Zhou, L., & Plemmons, A. (2006). Changes in scavenging of particles by droplets due to weak electrification in clouds. *Atmospheric Research*, *79*, 266–295.

Twomey, B. (1977). The influence of pollution of the shortwave albedo of clouds. *Journal of the Atmospheric Sciences*, *34*, 1149–1152.

Vali, G. (1985). Nucleation terminology. *Journal of Aerosol Science*, *16*, 575–576.

Wang, X., Zhang, L., & Moran, M. D. (2010). Uncertainty assessment of current size-resolved parameterizations for below-cloud scavenging by rain. *Atmospheric Chemistry and Physics*, *10*, 5685–5705. https://doi.org/10.5194/acp-10-5685-2010

Yang, F., Shaw, R. A., Gurganus, C. G., Chong, S. K., & Yap, Y. K. (2015). Ice nucleation at the contact line triggered by transient electro-wetting fields. *Applied Physics Letters*, *107*, 264101. https://doi.org/10.1063/1.4938749

Young, K. C. (1993). *Microphysical processes in clouds* (p. 427). UK: Oxford University Press.

Zhang, Liang (2017). Scavenging of particles by cloud droplets with varying particle density and relative humidity, (PhD dissertation). University of Texas at Dallas.

Zhang, L., & Tinsley, B. A. (2017). Parameterization of aerosol scavenging due to atmospheric ionization under varying relative humidity. *Journal of Geophysical Research: Atmospheres*, *122*, 5330–5350. https://doi.org/10.1002/2016JD026255

Zhou, L., & Tinsley, B. A. (2007). Production of space charge at the boundaries of layer clouds. *Journal of Geophysical Research*, *112*, D11203. https://doi.org/10.1029/2006JD007998

Zhou, L., & Tinsley, B. A. (2012). Time dependent charging of layer clouds in the global electric circuit. *Advances in Space Research*, *50*, 828–842.

Zhou, L., Tinsley, B. A., & Plemmons, A. (2009). Scavenging in weakly electrified saturated and sub-saturated clouds, treating aerosol particles and droplets as conducting spheres. *Journal of Geophysical Research*, *114*, D18201. https://doi.org/10.1029/2008JD011527

Zhou, L., Tinsley, B. A., Wang, L., & Burns, G. (2017). The zonal-mean and regional tropospheric pressure responses to changes in ionospheric potential. *Journal of Atmospheric and Solar - Terrestrial Physics*. https://doi.org/10.1016/j.jastp.2017.08.011